Mixture formation and combustion process analysis of an innovative diesel piston bowl design through the synergetic application of numerical and optical techniques

Authors

Millo, F., Piano, A., Roggio, S. (Politecnico di Torino, Italy)

Pastor, J.V., Micó, C., Lewiski, F.(CMT – Motores Térmicos, Universitat Politècnica de València, Spain)

Pesce, F., C., Vassallo, A. (PUNCH Torino S.p.A/ formerly General Motors Global Propulsion Systems, Italy)

Bianco, A. (Powertech Engineering Srl, Italy)

Abstract

The optimization of diesel engine piston bowl geometries has a crucial role in improving the near-wall flame evolution for better air/fuel mixing and soot reduction. With these aims, an innovative piston bowl for a light-duty diesel engine was designed, coupling both a sharp-stepped lip and radial bumps in the inner bowl rim. The impact of the proposed design was investigated through both 3D-CFD and single-cylinder optical engine. The numerical model, featuring a calibrated spray model and a detailed combustion mechanism, was used to analyse the non-reactive air/fuel mixing and the combustion processes. Results highlighted a reduced jet-to-jet interaction and better air/fuel mixing for the innovative bowl with respect to a conventional re-entrant design, thus enabling faster combustion process after the end of main injection. Numerical results in terms of flame's kinematic and oxidation process were validated against the combustion image velocimetry (CIV) and OH* chemiluminescence from the optical engine, showing higher velocity near the radial bumps, and faster flame recirculation towards the piston center. Moreover, both experiments and simulations showed a more intense OH distribution in the radial-bumps region and above the step during the first stage of the combustion process, thanks to the enhanced air/fuel mixing.

1. Introduction

One of the main concerns of society nowadays is the global warming. Different sectors, as energy, agriculture or industry are facing strict emission regulations to mitigate their impact and turning around the environmental situation. In this scenario, the transport industry is in the spotlight as global estimations indicate that 16% of the greenhouse gas emissions [1] are related to this sector, which is mainly powered by internal combustion engines (ICE) [2]. During the last decades, greats achievements have been reached in the ICE field, resulting in cleaner and more efficient technologies. Focusing on compression ignition (CI) engines, new combustion modes [3], new injection systems [4] and efficient after-treatment

strategies have contributed to important emissions reductions. In the last years, new research fields like alternative fuels or new piston geometries have stablished as promising and potential pathways to reduce soot formation inside the combustion chamber and improve the engine efficiency, while reducing the costs of after-treatment systems and the greenhouse gas emissions [5,6].

The piston geometry has an important influence on the NOx and soot formation in CI engines. The interaction between spray and wall directly affects the local air-fuel ratio and the flame movement inside the combustion chamber and, consequently, the soot formation and oxidation processes [6,7]. More specifically, the focus has been directed towards the soot oxidation during the late combustion phase [8,9]. A more efficient and faster oxidation process during this phase allows to use high exhaust gas recirculation (EGR) rates, reducing engine-out soot while not penalizing NOx emissions [10]. For light-duty CI engines, which are swirl-supported, re-entrant pistons are the most typical combustion chamber geometries employed. Based on this, new proposals have been developed to improve its performance. The stepped lip concept is one of the solutions that is being applied in modern diesel engines [6]. It is characterized by the presence of a chamfered lip at the top edge of the bowl, instead of the protruding lip used by the conventional re-entrant proposal. Instead of directing the sprays within the bowl, this design splits each spray into two parts. The upper part is directed towards the squish zone, improving the utilization of the air in this region [11]. Several benefits have been related to the use of the stepped lip geometry, as heat losses reduction, turbulence improvement, better air utilization and fuel consumption reduction in comparison with the re-entrant piston [8,12,13]. More recently, Mercedes Benz launched the OM654 engine, where the stepped lip concept is used. Fuel consumption and particulate emissions reductions were reported by the manufacturer [14]. Nevertheless, to fully exploit the beneficial mixing of flow structures obtained thanks to the stepped-lip bowl, an optimal spray targeting is required, as numerically evaluated in [11]. This result was also confirmed by Kurtz and Styron in [15], where the unbalanced fuel split on the step provided an engine efficiency worsening, especially at high load.

Recently, a new concept of piston has shown interesting results in heavy-duty engines. The concept was proposed by Volvo and consists on the introduction of protrusions (waves) uniformly distributed around the bowl circumference [9]. After the flame collides with the piston wall, the waves avoid the tangential movement and force it to move back towards the bowl center, where fresh oxygen is available. The flame-to-flame collision is smoothed due to the waves, reducing the formation of fuel-rich zones. Faster burn out and an impressive soot reduction (up to 80%) were reported. A remarkable fuel consumption reduction was also achieved by using this new piston geometry [16]. Recently, the potential of including radial protrusions have been numerically evaluated in a passenger car diesel engine: the innovative piston design showed a beneficial flatness in the trade-off curve over the EGR sweep at partial-load engine operating conditions

achieving 50% soot reduction and 5% BSFC improvement with respect to the re-entrant bowl [17]. A further step on the piston bowl optimization was carried out by Belgiorno et al. in [18], where an innovative geometry was obtained through additive manufacturing, coupling both a highly re-entrant sharp-stepped bowl and a number of radial protrusions in the bowl rim. The experimental activity on a single-cylinder engine showed an impressive soot reduction with any detrimental effects on fuel consumption [18]. For these reasons, it is considered of interest to evaluate the potential of introducing this novel concept in light-duty pistons. In this scenario, 3D-Computational Fluid Dynamics (3D-CFD) simulations play an important role on the definition of the guidelines for the piston optimization, featuring high predictive capabilities with remarkably lower time and cost resources compared to the experimental campaigns.

Considering all the above mentioned, the present work aims to evaluate the performance of a novel light-duty piston geometry proposal. Similarly to the piston bowl designed in [18], it combines two important features as stepped lip and radial protrusions, to improve the engine efficiency and soot reduction. For this purpose, a numerical study has been carried out following the simulation methodology described in [19]. This is based on an integrated and automated 1D-/3D-CFD coupling: the 1D-CFD models [20–22] were developed to provide both reliable injection rate and boundary conditions for the 3D-CFD initialization. In the first part of the research study, the non-reacting characterization of the mixing process was carried out through 3D-CFD simulations. Then, to significantly reduce the computational time, a sector-mesh of the cylinder geometry was built and used for the combustion simulation. CFD results have been validated with experimental data obtained from an optical engine based on the same engine, in which both combustion image velocimetry (CIV) and OH* chemiluminescence techniques were performed: on one side, CIV analysis was exploited for the validation of the numerical flow field under reactive condition; on the other side, the OH* chemiluminescence images were compared with the 3D-CFD OH mass fraction distribution in order to investigate the near-stoichiometric region of the flame. It is worth noting that just a qualitative comparison between 3D-CFD and experimental results was carried out due to the intrinsic differences in terms of layout (i.e., metal engine vs optical engine). In fact, the piston used for the optical access engine showed lower heat transfer due to lower quartz heat conductivity, and higher mechanical deformation [23]. Additionally, the optical engine was affected by a not negligible blow-by which was instead not modelled in the 3D-CFD analysis.

2. Simulation methodology

2.1 Test engine

The numerical analysis was carried out considering as a test case a light-duty diesel engine, whose main features are listed in Table 1. It implements a conventional re-entrant piston bowl, as depicted in Figure 1 – left, and it is equipped with a 8-hole solenoid injector.

Table 1. Test engine main features

Cylinders #	4
Displacement	1.6 L
Compression ratio	16:1
Turbocharger	Single-Stage with Variable Geometry Turbine (VGT)
Fuel injection system	Common rail Max Rail Pressure 2000 bar
Maximum power	100 kW @ 4000 RPM
Maximum torque	320 Nm @ 2000 RPM

The numerical simulations were performed for a partial load engine working point 1500 RPM x 4.6 bar of Indicative Mean Effective Pressure (IMEP). The 3D-CFD model for the conventional re-entrant piston bowl was extensively validated against the experimental data, highlighting a more than satisfactory accuracy in reproducing the combustion and emission formation processes, as reported in [19]. Once assessed the predictive capabilities of the simulation setup, an innovative piston bowl proposal was designed, named 'hybrid', featuring an annular recess step and a number of radial bumps equal to the injector nozzle holes in the inner bowl rim. The proposed combustion system has the same bore and squish height of the re-entrant bowl, while a compression ratio of 15 was set. Regarding the spray targeting, the injector protrusion within the cylinder was maintained unchanged. Figure 1 shows both piston bowl geometries under investigation.
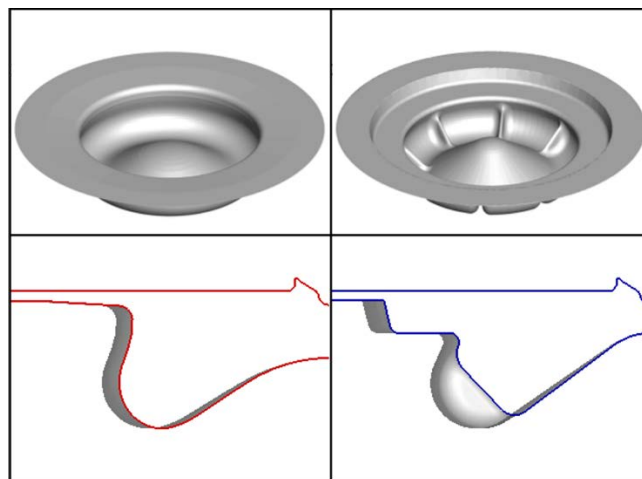

Figure 1. Piston bowl geometries under investigation. Left: re-entrant; right: hybrid

2.2 Simulation Setup

The CFD simulations were performed through the already developed 1D-/3D-CFD coupling methodology widely discussed in [19], whose main elements are reported here below. The 1D-CFD complete engine model, designed in GT-SUITE and validated in [20], provided the time-varying boundary conditions (thermodynamic state and species concentration) at the intake and exhaust ports. Then, a 3D-CFD simulation of the full cylinder engine (cold flow) was carried out in CONVERGE CFD, providing pressure, temperature and flow field in-cylinder evolutions during the gas exchange process. Starting from the intake valve closure , the compression stroke and combustion process were simulated for a single sector of the full cylinder geometry, centered along one spray axis. The injection rate was provided by a previously developed predictive 1D-CFD injector model [21,22]. The 3D-CFD results were thus post-processed through a GT-SUITE tool, providing the same solution methodology as the initial 1D-CFD complete engine model.

Regarding the 3D-CFD simulation, the Reynolds-averaged Navier-Stokes (RANS) based Re-Normalization Group (RNG) k-ε model [24] was adopted and the general settings are summarized in Table 2.

Table 2. Mesh Grid, Turbulence and Heat transfer models

Fixed embedding	Injector spray cone angle
Adaptive Mesh Refinement (AMR)	Velocity, temperature sub-grid criterion [25]
Grid size	0.50 mm (base grid) / 0.25 mm (AMR and fixed embedding)
Turbulence model	RNG k-ε model
Heat transfer model	O'Rourke and Amsden [26]

For the spray model, the "blob" injection method was employed [27] with a calibrated Kelvin Helmholtz and Rayleigh Taylor (KH-RT) breakup model [27]. The main elements of the spray model are listed in Table 3.

Table 3. Spray sub-models

Discharge coefficient model	Cv correlation [25]
Breakup model	Calibrated KH-RT
Turbulent dispersion	O'Rourke model [28]
Collision model	No Time Counter (NTC) collision [29]
Drop drag model	Dynamic drop drag [30]
Evaporation model	Frossling model [28]
Wall film model	O'Rourke [31]

As far as the combustion model is concerned, the SAGE detailed chemical kinetics solver was adopted, while the soot mass was predicted by means of the detailed Particulate Mimic (PM) soot model [32–34]. Table 4 summarizes the key elements for the combustion simulation.

Table 4. Fuel surrogate, reaction mechanism and emissions models

Fuel surrogate	N-Heptane
Reaction Mechanism	Skeletal Zeuch [35]
Species	121
Reactions	593
Soot precursor chemistry	Embedded in the reaction mechanism
Poly-cyclic Aromatic Hydrocarbons (PAH)	(A3R5-)
Soot model	Particulate Mimic (PM)
NOx chemistry	Embedded in the reaction mechanism

3. Experimental methodology

3.1 Engine and Test cell

Tests were performed in an optically accessible single cylinder CI engine, with the aim of validating CFD simulation results. It is based on the same architecture as the one used for simulations. It has 402 cm^3 displacement as the stroke and bore were kept like the original multi-cylinder platform. Additionally, the engine is equipped with the same cylinder head as the original one, with four valves and a centred solenoid injector per cylinder. The main parameters of the optical engine are summarized in Table 5. More details of the facility can be found in [36]. It is important to highlight that the compression ratio of this engine is lower than the one used in simulations. It is caused by a lower position of the piston rings in comparison to a conventional engine, to avoid the lateral optical accesses when the piston is at Top Dead Center (TDC).

Table 5. Optical engine main features

Cylinders #	1
Displacement	402 cm3
Bore x Stroke	80 mm x 80.1 mm
Compression ratio	12.5:1 (re-entrant)/11.5:1(hybrid)
Valve #	4

The heat plug from the cylinder head was replaced by a piezoelectric pressure transducer (AVL GH13P) to measure instantaneous in-cylinder pressure. This signal is used to calculate the Heat Release Rate (HRR). An in-house developed tool was utilized for this purpose, which is based on the application of first law of thermodynamics to the in-cylinder volume [37]. It is applied in the range between intake valve closing and exhaust valve opening and considers wall heat transfer, blow-by and mechanical deformations. A detailed characterization of this engine can be found in [23].

The optical access is based on the use of a Bowditch piston, equipped with a fully transparent piston head (Figure 2). To mimic the flow dynamics of the original metal engine, two different models were used based on realistic bowl geometries. The first one has a conventional re-entrant bowl (Figure 1 – left). The second one combines two different geometries: one half of the piston has the hybrid geometry (Figure 1 – right), including both the annular recess step and the radial bumps, as shown in Figure 1 – right; the other half of the piston has only the recess step.
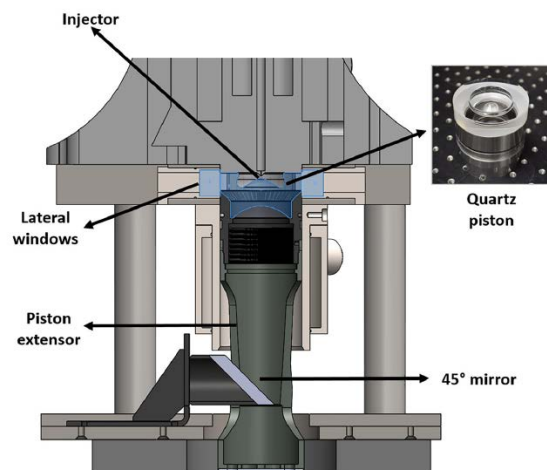

Figure 2. Representation of the optical engine. Adapted from [36].

A Schenck electric dynamometer (220kW and 562nm) is used to control engine load and speed. Additionally, the test cell allows controlling intake air pressure and temperature [36]. A screw compressor supplies pressurized air, which is dried and heated before reaching the intake ports. A backpressure regulator is used to control exhaust pressure. Pressure pulses either in the intake or the exhaust line are avoided thanks to the presence of settling chambers just upstream and downstream the engine.

Test were performed at 1250 RPM x 4.5 bar IMEP. Due to the different compression ratio of the pistons (see Table 5), intake temperatures and pressures were adjusted to achieve the same engine load in both cases. On the other hand, the mass of fuel injected and the in-cylinder peak pressure were kept constant. In this way, similar thermodynamic conditions were guaranteed for both pistons. The intake operating conditions are summarized in Table 6. The engine

is operated under skip fire mode to minimize window fouling and thermal stresses, as well as piston ring deterioration. Thus, fuel injection takes place one out of 20 cycles.

Table 6. Engine intake operating conditions

Piston geometry	Intake Press. (bar)	Intake Temp. (°C)	$\dot{m}_{air}$ (g/s)
Re-entrant	1.9	90	7.26
Hybrid	2.1	120	7.55

The fuel is supplied by a conventional fuel pump into a common rail system, while the injector is controlled by a DRIVVEN® control unit which allows to perform complex injection strategies. As in numerical activity, injection strategy features four different pulses (pilot 1, pilot 2, main and post-injection) with an injection pressure equal to 670 bar.

3.2 Optical techniques

3.2.1   Combustion Image Velocimetry

The CIV technique is based on the use of in-cylinder thermal radiation images to characterize the flame (soot) movement. The processing algorithm applied for this purpose is the same as the one used in Particle Image Velocimetry (PIV). The main difference is that PIV requires to seed in-cylinder flow with particles and illuminate them with an external light source (laser sheet), while for CIV the incandescent soot acts as the tracking source. This technique has been previously applied in different studies [8], where the use of realistic bowl geometries and/or reactive conditions hinder the application of conventional PIV.

The thermal radiation emitted by soot was registered by a high-speed CMOS camera (Photron SA-5), coupled to a Carl Zeiss Makro-Planar camera lens (100mm, f/2). It was set to record at 25.000 frames per second with an exposure time of 6.65 μs. The image size was 512 x 512 pixels with 8.1 pixel/mm resolution.

A cross-correlation algorithm was applied to obtain instantaneous 2D velocity distributions. It must be noted that images are formed by radiation emitted by the whole soot cloud (a three-dimensional object). Therefore, it is difficult to relate the observed movement with a certain measuring plane. Image processing was carried out with PIVlab software [38]. Time interval between images was 40 μs and the interrogation area varied from 32x32 to 16x16 pixels.

3.2.2   OH* Chemiluminescence

The radiation emitted by the excited-state OH* can be used to visualize the near-stoichiometric reaction regions. In this work, an intensified ICCD camera (Andor Solis iStar DH334T-18H-83) was used, equipped with a Bernhard-Halle UV lens (100mm, f/2). This set provided 1024 x 1024 pixels images with 8.75 pixel/mm resolution. A bandpass filter was mounted in front of the camera to reject radiation from other sources. It had a transmission spectrum centred at 310nm with 20nm full width half maximum. Radiation was registered at 6 different crank angle degrees during the combustion process, with an acquisition rate limited to 1 frame per cycle.

4.   Results and discussion

4.1 Flow structures and air/fuel mixing

Before analysing the combustion phenomena and comparing the numerical results with the experiments, the effects on the in-cylinder flow field and the mixture formation were assessed by means of CFD non-reacting simulations for the whole cylinder geometry. Thanks to this analysis the spray/wall interaction was investigated, avoiding the combustion influence on turbulent structures. Starting from a macroscopic point of view, the time evolution of the swirl ratio (SR) and the injection rate profile for each combustion system are shown in Figure 3.
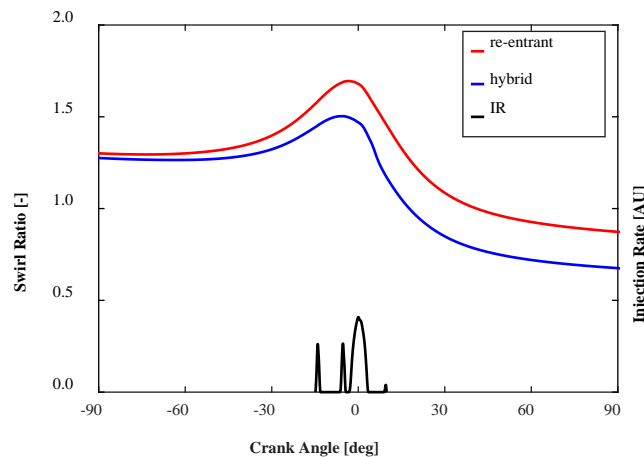

Figure 3. Swirl ratio and injection rate profile for the analyzed combustion systems. Engine operating condition: 1500 RPM x 4.6 bar IMEP

Close to the TDC, the re-entrant bowl highlights higher swirl amplification with respect to the hybrid bowl. Indeed, two competitive phenomena for the hybrid bowl result in lower swirl ratio during the compression stroke. On one side, the lower squish area for the hybrid bowl, as outlined in Figure 1, leads to a reduced squish flow intensity which is responsible for a lower swirl amplification, as also reported in [39]. On the other side, the radial bumps break the rotational swirling flow, limiting the swirl intensity. To further understand the radial bumps effects on the swirl motion, the velocity flow

field was investigated at the Start of Injection (SOI) on a plane Z cutting the radial bumps in the upper region. For this purpose, Figure 4 shows at -14 CAD aTDC the tangential component of the velocity vectors contained in the selected plane Z, called projected velocity, with uniform size and coloured according to the magnitude.
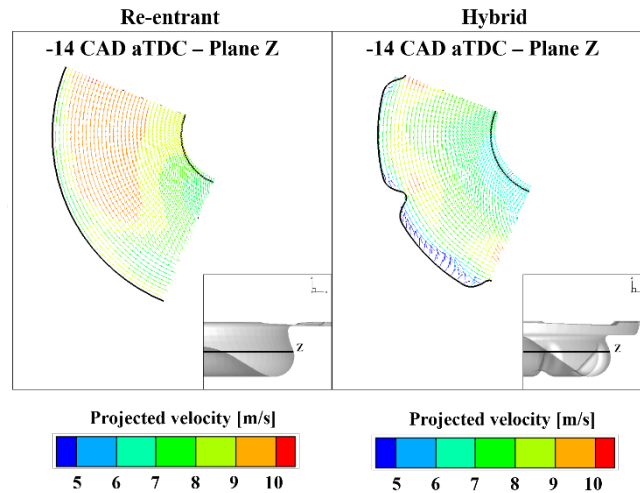

Figure 4. Velocity vectors at -14 CAD aTDC coloured according to the magnitude of the projected velocity on the selected plane Z. Left: re-entrant; right: hybrid. Engine operating condition: 1500 RPM x 4.6 bar IMEP

The flow field for the re-entrant bowl is supported by swirl motion, differently from the hybrid bowl where the flow structure is strongly affected by the radial bumps. The flow separation occurring on the bump tip enhances the formation of highly turbulent structures, while the gas within two adjacent radial bumps is slowed down, creating a "stagnation zone".

The combustion system effects on the velocity flow field was furtherly investigated after the End of Injection (EOI) of the main event. Three different horizontal planes, parallel to the cylinder head, were selected to show the corresponding projected velocity. The plane Z1 refers to the step region, while both plane Z2 and plane Z3 are in the radial bumps region, respectively in the upper and lower part. The projected velocity in the selected planes at +5 CAD aTDC are shown in Figure 5.
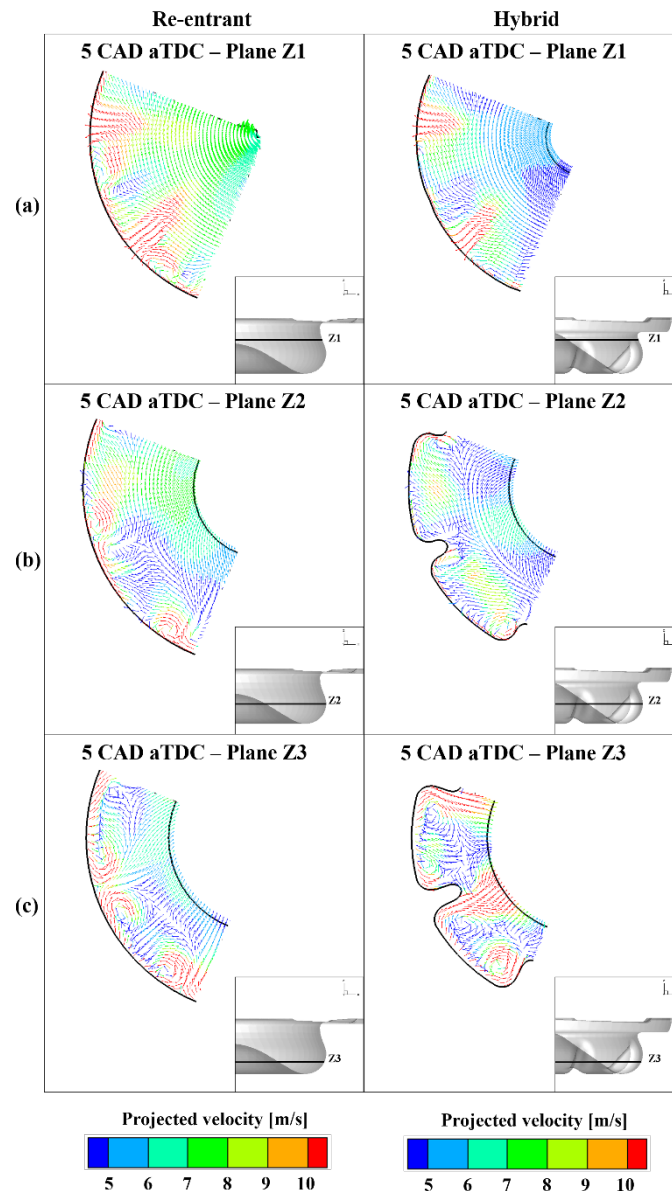
Figure 5. Velocity vectors at +5 CAD aTDC coloured according to the magnitude of the projected velocity on the selected cutting planes Z1 (a), Z2 (b) and Z3 (c). Left: re-entrant; right: hybrid. Engine operating condition: 1500 RPM x 4.6 bar IMEP

As far as the plane Z1 is concerned, the overall flow structure is swirl supported for both the combustion systems, although the swirl vortex for the hybrid bowl has lower intensity, as depicted in Figure 5 – a. Additionally, the jet-to-jet interaction with the hybrid bowl is clearly minimized due to the spray split on the step, that reduces the spray tangential propagation and redirects the jet upward above the step. The radial bumps effects on the flow structures can be clearly observed on the plane Z2 in Figure 5 – b. The hybrid design strongly affects the swirling flow, breaking its organized macro-structure between two adjacent bumps. Near to the bumps tip, the high jet momentum is redistributed as vortices over the bump profile. Consequently, the jet-to-jet interaction is efficiently reduced respect to the re-entrant bowl. Moving toward the plane Z3 (Figure 5 – c), the jet-to-jet interaction for the re-entrant bowl is clearly evident and it is driven by the formation

of two counter rotating vortices. While, the bottom-bump curvature in the hybrid bowl promotes the fuel jet redirection towards the bowl center. However, due to the swirl motion, the spray/wall event occurs asymmetrically near to the bump region.

The combustion systems behaviour in terms of mixing process was further analyzed, investigating the equivalence ratio contour plot after the main EOI (+5 CAD aTDC) for each piston bowl under investigation, as shown in Figure 6. As already stated, considering the plane Z1 of Figure 6 – a, the re-entrant bowl shows a more intense jet-to-jet interaction than the hybrid design in the step region. Focusing on the upper region of the radial-bumps (Figure 6 – b), the tangential fuel jets propagation along the bowl surface is noticeably different with respect to the one obtained with the re-entrant bowl. The radial bumps minimize the jet-to-jet interaction and the fuel plumes are driven to the bowl center by the bump, and then guided by the swirl motion into the consecutive sector, as highlighted by the black arrow. Consequently, the available high oxygen concentration in the adjacent sector due to the asymmetrical spray-wall interaction, can efficiently enhance the air/fuel mixing onto the jets front. The different fuel jets evolution could be also highlighted in the bottom-bump region (Figure 6 – c). Again, it is worth to note the importance of the radial bumps in limiting the jet-to-jet interaction. The fuel plumes propagation toward the bowl center is remarkably enhanced for the hybrid bowl, as confirmed by the higher fuel concentration within the black circle. Indeed, as mentioned before, the lower swirl ratio allows a higher spray momentum transfer along the bowl surface. This is mainly redistributed as a more intense tumbling vortex which efficiently drives the fuel plumes toward the bowl center, and enhanced by the higher bowl curvature in the dome region (see Figure 1). The available oxygen placed in the piston bowl center can therefore effectively improve the air/fuel mixing onto the jets front.
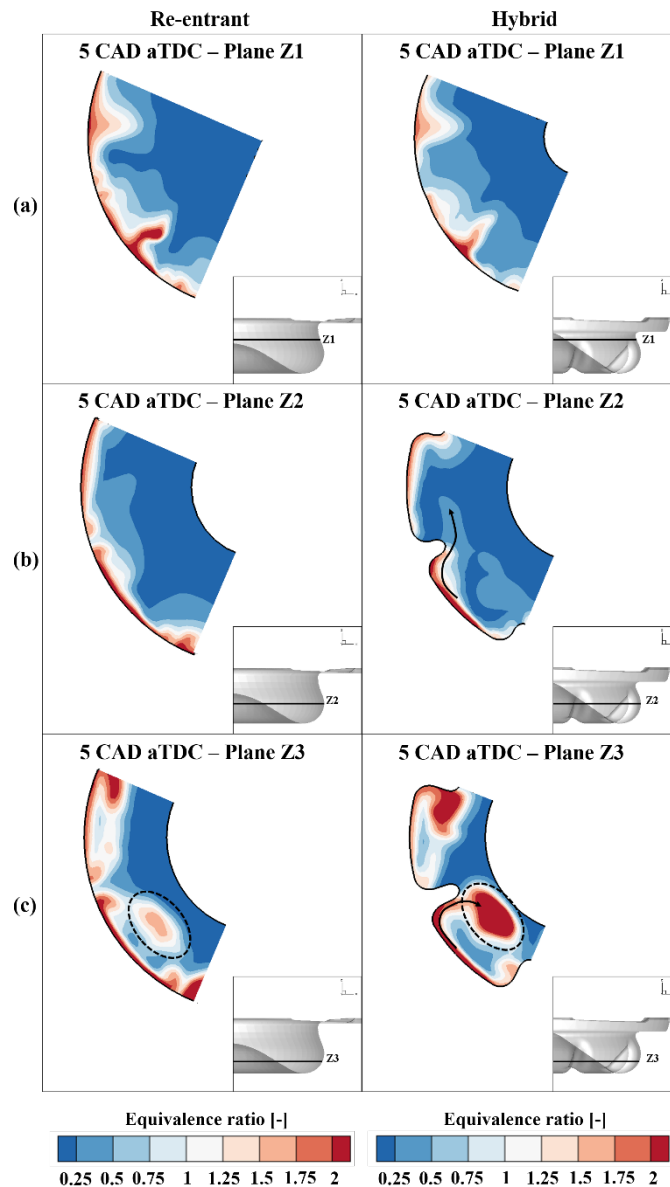
Figure 6. Equivalence Ratio contour plot at +5 CAD aTDC on the selected cutting planes Z1 (a), Z2 (b) and Z3 (c). Left: re-entrant; right: hybrid. Engine operating condition: 1500 RPM x 4.6 bar IMEP

The equivalence ratio distribution was further investigated during the post injection event (+10 CAD aTDC) as shown in Figure 7. During post injection, the more intense tumbling vortex for the hybrid bowl moves the fuel plumes toward the bowl center. This is clearly evident by looking the plane Z1 in Figure 7 – a, where a fuel rich cloud can be observed close to the bowl center. The effects of the high tumbling vortex intensity coupled with the radial bumps are undoubtedly relevant: differently from re-entrant concept in which the lower curvature and the absence of the radial bumps merge two adjacent fuel plumes without redirecting them toward the dome, the hybrid bowl drives the fuel to the bowl center, keeping separate fuel jets, thus avoiding extremely fuel rich region, as shown in Figure 7 – b. Therefore, a slower and less efficient air/fuel mixing rate is expected for the re-entrant bowl during the late phase of the injection event. As far as the bottom-bump region is concerned (plane Z3 in Figure 7 – c), both the piston bowls show the higher fuel concentration close to

the piston dome. However, the fuel rich cloud for the hybrid bowl is remarkably reduced thanks to the tumbling vortex enhanced by the higher bowl curvature and the lower opposed swirl motion.
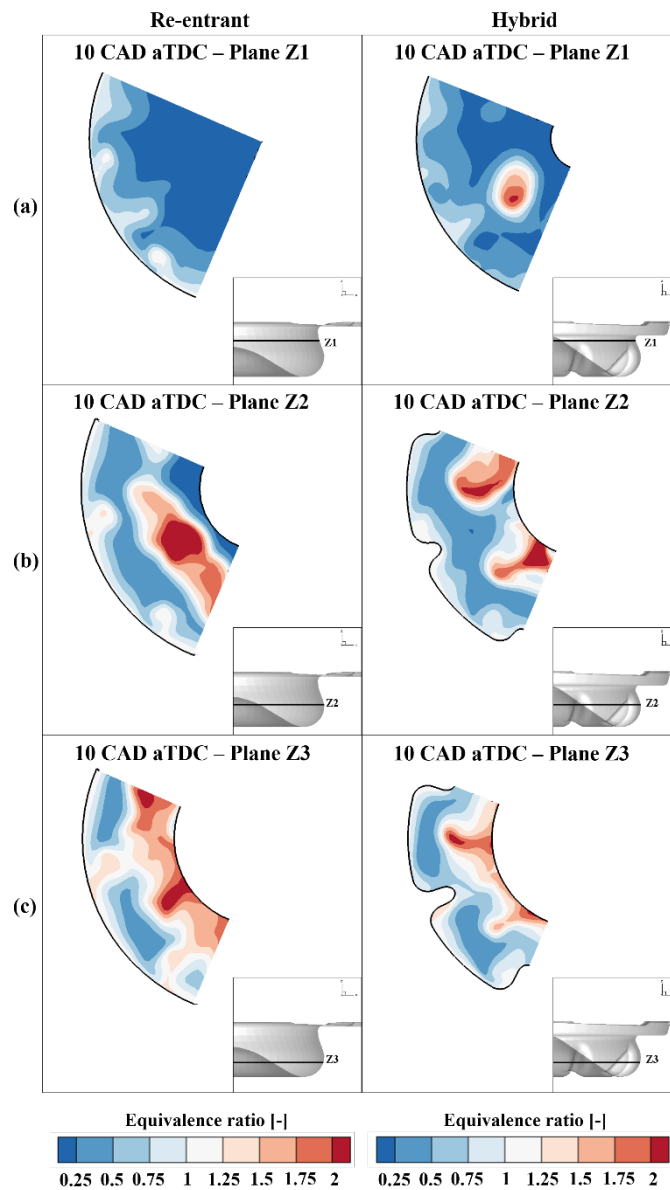

Figure 7. Equivalence Ratio contour plot at +10 CAD aTDC on the selected cutting planes Z1 (a), Z2 (b) and Z3 (c). Left: re-entrant; right: hybrid. Engine operating condition: 1500 RPM x 4.6 bar IMEP

To globally characterize the mixing process induced by different piston bowl geometries, a mixing rate index was defined based on the equivalence ratio distribution during the injection event, as already reported in [17]. For the purpose, the total cylinder mass was binned by equivalence ratio into twenty intervals from 0.0 to 2.0, in which 0.1-0.2 bin represents the intake flow (pure ambient gas combined with EGR), while the 1.9-2 bin corresponds to the injected fuel mass. Then, the cylinder mass fraction for each bin was traced on bar chart and a contour plot was designed gathering all the bar chart for each crank angle, as outlined in Figure 8. This representation can properly indicate the rate of air/fuel mixing, since

the higher the cylinder mass fraction in the range 0.2-1, the more efficient the air utilization within the combustion chamber. Up to the end of main injection (from -15 to +5 CAD aTDC), the air/fuel mixing is mainly represented by the free spray evolution. Hence, no significant differences can be observed in the equivalence ratio distribution between the two combustion systems. Nevertheless, when the jet-to-jet interaction occurs, the air utilization in the collision area of the re-entrant design is minimized resulting in lower air/fuel mixing rate, as also confirmed in [16]. As previously described in Figure 6, the re-entrant bowl shows at +5 CAD aTDC a remarkable interaction between adjacent fuel plumes, while it is avoided in the hybrid bowl that promotes the formation of different recirculating structures, depending on the bump region. As expected, these mechanisms lead to a faster air/fuel mixing, increasing the cylinder mass fraction in the equivalence ratio range 0.3-0.6. This effect becomes more important going toward the end of post injection event, close to +10 CAD aTDC, in which the hybrid bowl highlights the higher cylinder mass fraction within the 0.3-0.8 equivalence ratio bins. Additionally, after the post EOI, the enhanced mixing mechanism with the hybrid bowl promotes the faster spreading of the cylinder mass fraction toward the stoichiometric range.
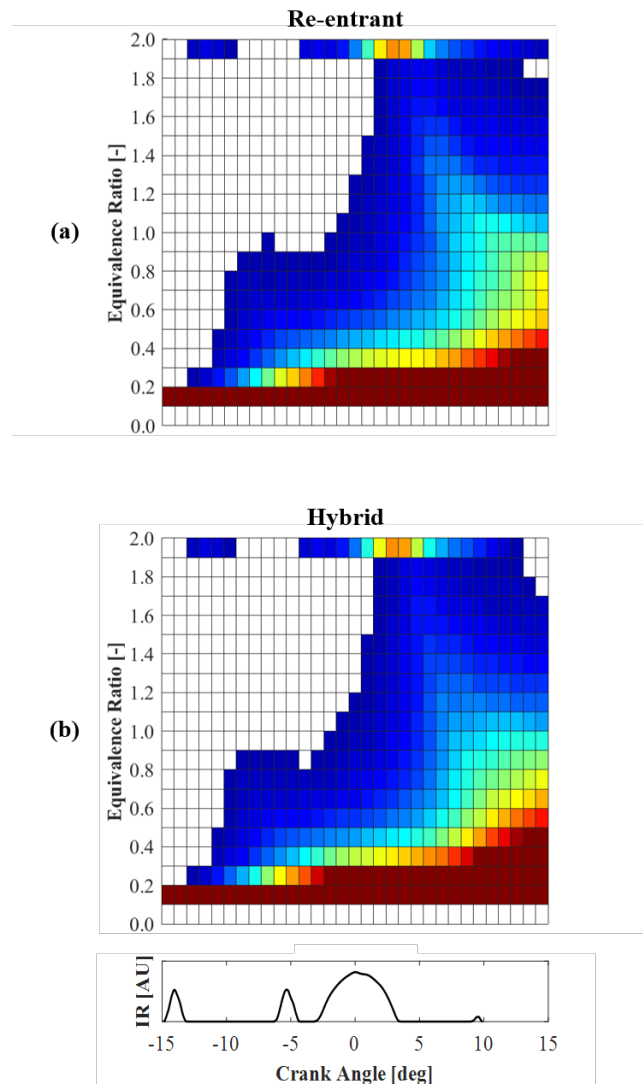
Figure 8. Cylinder mass fraction evolution for each equivalence ratio bin. (a) re-entrant; (b) hybrid. Engine operating condition: 1500 RPM x 4.6 bar IMEP

4.2 Combustion analysis

Once assessed the mixing process, the influence of the piston bowl design on the combustion was investigated, following the simulation methodology previously described. The numerical results were validated against the experimental data from the optical access engine considering similar operating conditions, both in terms of injection strategy and IMEP. Although there are undoubted differences between the real metal engine and the optical access engine, the qualitative comparison between experiments and numerical results was deemed extremely important to highlight, firstly, the prediction capability of the developed model and, secondly, to confirm that the observed phenomena could be extended in real engine operating conditions. Last but not least, an innovative methodology to directly compare the numerical results with the experimental data from optical engines was developed.

Figure 9 shows the simulated HRR for both the bowl geometries under investigation. During the free flame development of the first pilot injection event, no significant differences can be highlighted between the two designs. At this stage, the injection pressure drives the air entrainment and thereby the bowl effect on the combustion rate is negligible. Moving toward the TDC, the premixed combustion due to the second pilot injection enhances the HRR for the re-entrant bowl. In this phase, the flame-to-wall event and the resulting loss of kinetics reduce the mixing rate onto the flame front, as also noted in [16]. The reduced swirling flow for the hybrid bowl slightly affects the spray development, increasing the flame/wall interaction and thus reducing the combustion rate. The same behaviour can be observed for the experimental HRR of Figure 10, confirming the predictive capabilities of the numerical models. The flame/wall effects become particularly evident for the premixed combustion phase of the main injection. Both the numerical and the experimental HRR outline a steeper rate of combustion for the re-entrant bowl, resulting in the higher peak of HRR respect to the hybrid bowl. However, after the main EOI, the flame-to-flame interaction occurred in the case of re-entrant bowl (see Figure 6) causes a HRR drop under the one obtained with the hybrid bowl. Conversely, in this latter the mitigation of the flame-to-flame event due to the radial bumps and the enhanced mixing mechanisms, already pointed out, promote a faster combustion process. During this phase, the numerical results show an excellent agreement respect to the experimental data, capturing the timing when the change in slope for the re-entrant HRR occurs. After the post EOI, during the late phase of the combustion process, the numerical HRR obtained for the re-entrant bowl rises over than with the hybrid bowl due to the higher swirl ratio that efficiently enhances the mixing of the residual fuel, as experimentally confirmed in Figure 10, suggesting once again the reliability of the developed CFD models.
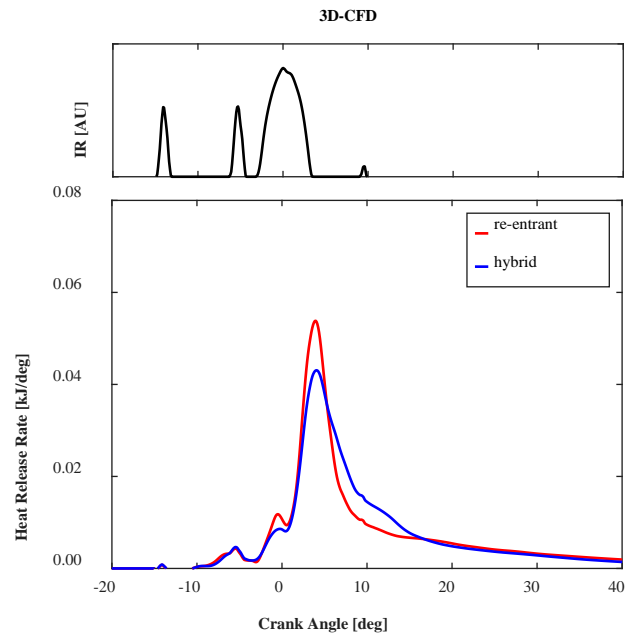
Figure 9. Numerical results for the tested metal engine. Top: injection rate profile; bottom: Heat Release Rate. Engine operating condition: 1500 RPM x 4.6 bar IMEP
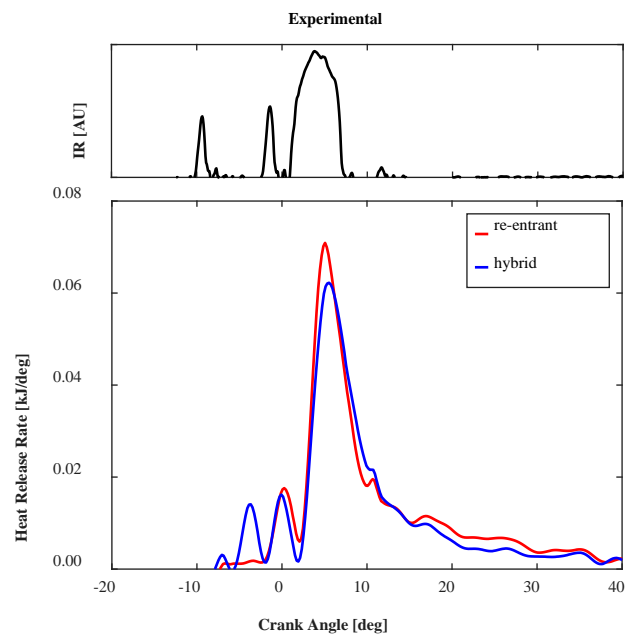

Figure 10. Experimental results for the optical access engine. Top: injection rate profile; bottom: Heat Release Rate. Engine operating condition: 1250 RPM x 4.5 bar IMEP

Flow field under reactive condition

As previously highlighted, the combustion simulations show a more than satisfactory accuracy on reproducing the HRR of the experimental tests. However, exploiting the potential benefits of the optical access engine, a further step on the validation process was performed evaluating the velocity field during the combustion process. With this aim, numerical

results from a single cylinder sector were compared with the outcomes from the CIV analysis, adopted in the optical engines to provide qualitative information of the main flow structures for each piston bowl. Therefore, to compare the experimental and numerical flow fields, the CFD velocity field was averaged along the cylinder axis, following the methodology described in [40]. More specifically, the average was preformed considering the volume from a specific distance from the cylinder head and the bowl surface to avoid the spray core effect on the flow field. During the injection event (+3 CAD aEOI of main event, Figure 11), CFD velocities show a good correlation with CIV data for both the investigated designs. The overall velocity magnitude for the re-entrant bowl is higher than the one observed with the hybrid bowl, that redirects part of the fuel jet momentum above the step. Two qualitative regions can be identified for both the piston bowls. Near the cylinder axis the flow is swirl supported for both the designs, but the re-entrant highlights a more intense macro-vortex with respect to the hybrid. In this region, the experiments show higher velocity magnitude due to the spray impact on the overall flow field that is partly avoided in the CFD thanks to the previously mentioned methodology. In the bowl periphery the flame propagation toward the center (reverse flow) is predominant. Both the piston bowls highlight the high-magnitude velocity in this region, where the reverse flow guides the flame front toward the piston center. However, this effect is emphasised by the radial bumps as outlined by the high-magnitude velocity vectors closer to bowl center (Figure 11 – right).
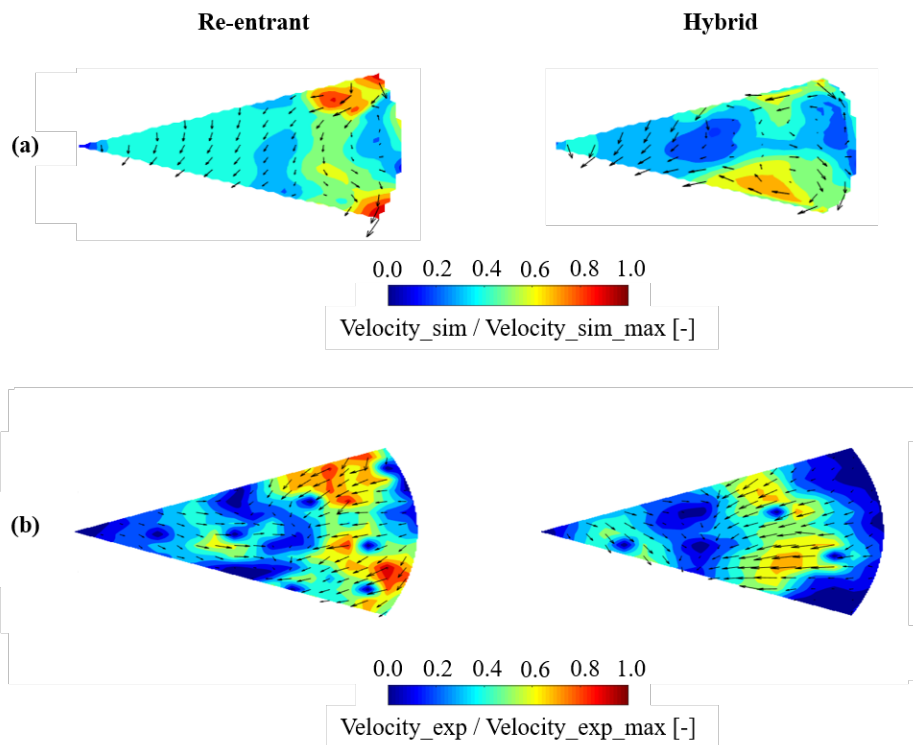

Figure 11. 3D-CFD z-average velocity (a) and experimental CIV-resolved velocity flow field (b) at +3 CAD aEOI of main event. Left: re-entrant; right: hybrid

After post EOI (+25 CAD aTDC, Figure 12), CFD and CIV flow fields show a fairly good agreement considering the total cylinder volume as average-path (in this case, flow field is not affected by any injection event). At this stage, the flow motion within the re-entrant bowl is mainly swirl supported; contrarily, macro-vortex structure cannot be visualized for the hybrid bowl since the velocity vectors are mainly directed toward the bowl periphery, due to the more intense tumbling vortex which drives the leading edge of the flame outward above the step region. This behaviour can be observed both in the experimental and CFD velocity fields, confirming that the numerical methodology can qualitative reproduce the experimental CIV-resolved flow, crucial for the proper prediction of the soot-oxidation process in the late cycle.
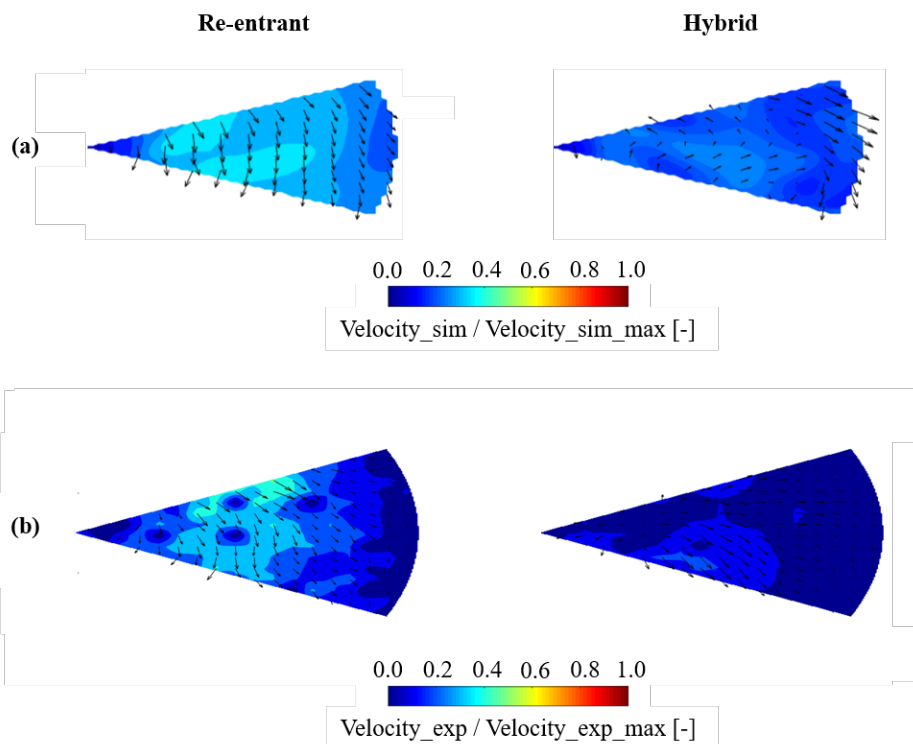

Figure 12. 3D-CFD z-average velocity (a) and experimental CIV-resolved velocity flow field (b) at +25 CAD aTDC – Late oxidation phase. Left: re-entrant; right: hybrid

In order to investigate the piston bowl effect on the velocity field during the combustion process, a time- and spatial-resolved velocity magnitude map representation was considered. Specifically, the two bowls were divided in angular sectors and the velocity in each sector was averaged. Following this procedure, a 2D contour-map was defined as shown in Figure 13, where the evolution of velocity as a function of sector location and crank angle degree is represented for both simulations (a) and experiments (b). As far as numerical distribution is concerned, to avoid the spray core impact on the CFD flow field, the velocity in each sector was averaged considering only the cell in the domain in which the temperature was higher than 1500K, thus considering only the burned gas. On the y-axis in Figure 13 is shown the azimuthal coordinate of a bowl sector: 0 and 45 represent the axis of two adjacent radial bumps. Considering the CFD

results, in Figure 13 – a, both the piston bowls highlight near the main EOI a high-magnitude velocity region. Close to the end of main event, the injection interaction with the bowl surface leads to higher tangential velocity, especially for the re-entrant bowl. Instead, a lower tangential velocity can be observed for the hybrid bowl, since the fuel jet momentum is redistributed above the step. This behaviour is confirmed by the experimental 2D-map in Figure 13 – b. Moving ahead in the cycle, the velocity magnitude is attenuated especially for the hybrid bowl and different velocity distribution can be highlighted. More in details, the intense swirl vortex for the re-entrant bowl (as depicted in Figure 3) leads to a directional flow from 0 to 45 sector angle as shown in Figure 13 – left. As far as the hybrid bowl is concerned (see Figure 13 – right), the peak of velocity magnitude is lower with respect to re-entrant design. In addition, the high-velocity region is localized near 0 and 45 sector angles, where the radial bumps are placed, while map center, related to the sector bowl axis, is characterized by a low velocity magnitude. This is due to the flame propagation toward the bowl center which is mainly driven by the radial bumps. From +8 CAD aEOI of main event, the re-entrant bowl highlights higher velocity magnitude than the hybrid bowl in the whole 2D contour-map, both for the numerical and experimental results, since at this stage the radial bumps reduce the swirl vortex.
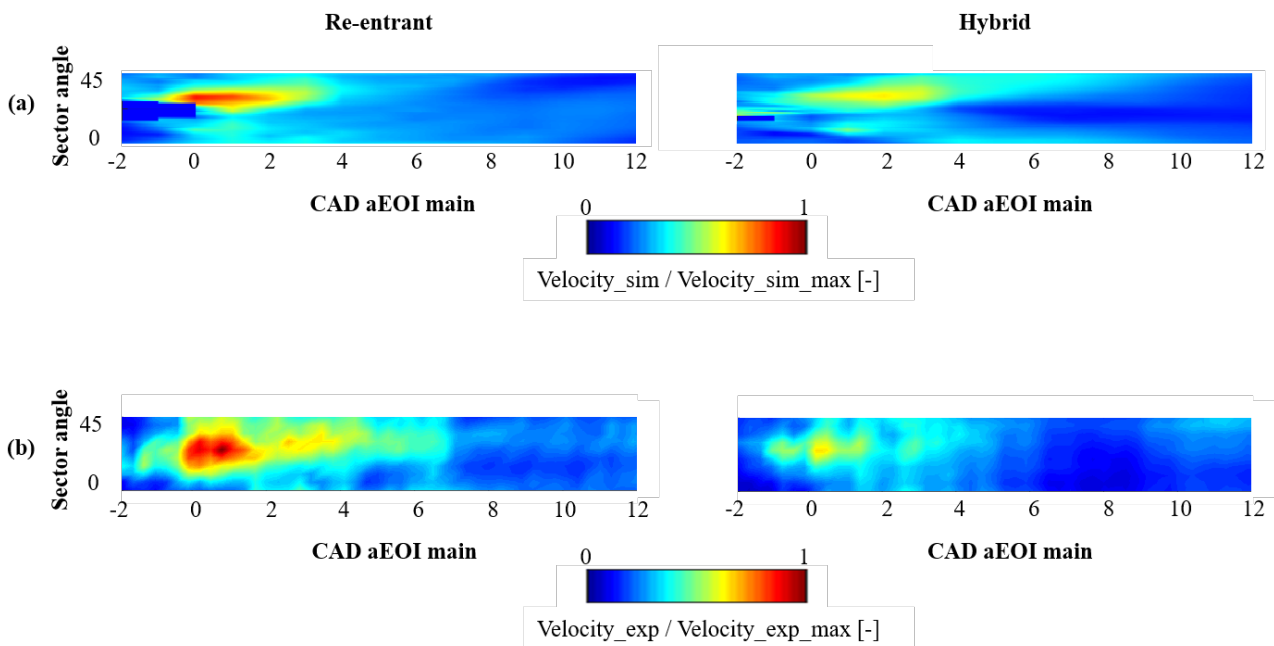

Figure 13. Average velocity evolution for each sector angle. (a) 3D-CFD; (b) experimental CIV-resolved

OH evolution

To fully characterize the combustion process in the near-stoichiometric high temperature flame front, the evolution of OH radicals was analyzed through CFD simulations and validated against the experimental OH* chemiluminescence images. Firstly, total OH mass as a function of crank angle degree for each investigated bowls is shown in Figure 14. Up to the EOI of main event, when the OH is mainly localized around the spray core, the piston bowls highlight comparable

OH mass. Moving toward the SOI of post event, the hybrid bowl enables faster oxidation process thanks to its optimized geometrical features, as confirmed by the higher peak of OH mass. The radial bumps affect the flame diffusion toward the piston center, increasing the air/fuel mixing. Moreover, higher OH content is expected in the squish region thanks to the better air utilization above the step. From the EOI of post event, the higher oxidation rate for the hybrid bowl results in faster burn-out of the residual fuel and consequently lower OH mass is shown respect to the re-entrant bowl.
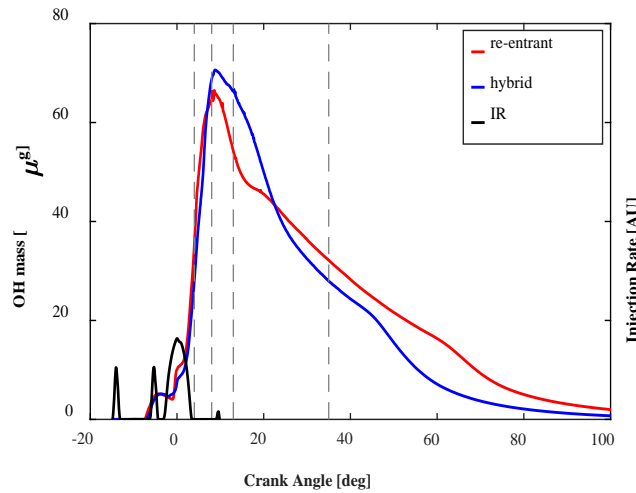

Figure 14. Numerical OH mass evolution and injection rate profile. Engine operating condition: 1500 RPM x 4.6 bar IMEP

After that, thanks to the adoption of SAGE coupled with the detailed chemistry, the OH mass fraction (yOH) planar distribution over the whole computational domain was computed. With this aim, the yOH was firstly traced and then each cell-value was averaged along the cylinder axis direction following Equation 1:

$$yOH_{i,j} = \frac{1}{N} \sum_{k=1}^{N} yOH_{i,j,k}$$ Eq. 1

where i, j, k represent the location of each cell in terms of x, y, z and N represents the total number of cell along the z-axis with not null $yOH_{i,j,k}$. This methodology allows the comparison between the numerical results with the OH* chemiluminescence images obtained by means of optical engine, and it is reported in Figure 15 (a and b, respectively) for the crank angle degrees highlighted in Figure 14. It is worth to note that, since the numerical and experimental injection schedules are slightly different, the experimental OH images refer to the same CAD interval after main end of injection of the CFD analysis.

At $\theta_1 = +0$ CAD aEOI of main event

As highlighted in Figure 15 – a, the combustion systems show similar OH distribution which is mainly localized in the region where the flame/wall interaction occurs, resulting in a comparable total OH mass for both the piston designs (see Figure 14). However, some differences can be observed within the bowl and outward in the squish region. The re-entrant bowl shows a more intense flame-to-flame interaction, as confirmed by the higher OH magnitude in the collision area of two adjacent flames. Contrarily, with the hybrid bowl the consecutive flames are more separated, promoting the faster combustion rate previously discussed. Focusing on the squish region, only the hybrid bowl leads to high OH content thanks to the lip interaction. As far as the experimental results of Figure 15 – b are concerned, an overall good agreement with the numerical results can be observed. In the re-entrant bowl, most of the adjacent flames interact and, contrarily to the numerical results, a unique circular flame front strongly propagates outward in the squish region. It is worth to note that this discrepancy is mainly due the retarded injection in the experiments with respect to simulations that leads to higher fuel split above the bowl lip. For the hybrid bowl, both numerical results and experiments show same behaviour: the flame-to-flame interaction is significantly minimized (only one spray plume ignites well-separated from the adjacent jet) and the flame propagates outward in the squish region thanks to the lip interaction.

At θ_2 = +4 CAD aEOI of main event

At +4 CAD aEOI of main event , the flame-to-flame interaction for the re-entrant bowl is particularly evident, as depicted in Figure 15 – a. The collision area between two consecutive flames (moved by the swirl motion) propagates toward the cylinder axis. While, the flame front in the squish region starts to move toward the liner. Considering the hybrid bowl, the flame-to-flame interaction is minimized and the shape of the collision zone is quite different respect to the re-entrant bowl. In fact, the flames interaction is only occurring in the sector periphery on the step, where the bumps absence cannot affect the flame-to-flame event. Furthermore, the fuel split on the step improves the air utilization in the squish region, enhancing the oxidation rate as confirmed by the higher global OH mass of Figure 14. Focusing on the OH* chemiluminescence images of Figure 15 – b, some discrepancies in comparison with the numerical OH distribution can be observed, as highlighted by the region within the red dashed line. More in details, the radiation obtained for the re-entrant design within the bowl are visibly lower than the hybrid bowl. This luminosity mitigation is mainly related to the higher soot content near the wall surface where flame-to-flame event occurs, that can significantly increase the absorption of the OH radiation, as experimentally found in [36]. The hybrid bowl, on the other side, shows a negligible luminosity attenuation since the radial bumps, separating each flame, limit the soot formation near the wall surface. Therefore, the OH* chemiluminescence image shows a fairly good agreement with the numerical OH distribution, in which the soot attenuation is not computed.

At θ_3 = +8 CAD aEOI of main event

After the end of post injection event, as shown in Figure 14, the total OH mass for the re-entrant bowl is lower than with the hybrid bowl, suggesting a reduced oxidation rate in the flame front. At this stage, the flame diffusion toward the piston center (reverse flow) mainly guides oxidation process. Specifically, as presented in Figure 15 – a, the OH concentration for the re-entrant bowl is mainly placed near the outer bowl rim and in the squish area. Instead, for the hybrid bowl two high-OH regions can be highlighted: on one side, an intense OH zone appears remarkably advanced toward the piston dome, due to the radial bumps effect on the flame; on the other side, thanks to the step geometry, the flame propagates above the step and recirculates inward within the bowl, limiting the flame propagation toward the cylinder liner [17]. This is confirmed by the higher OH concentration in the bowl periphery respect to the re-entrant bowl, suggesting a higher combustion rate in the step region. As far as the CFD prediction is concerned, the numerical OH distribution at θ_3 is again well-matched with the experiments for both combustion systems. More specifically, coherently with the CFD results, the hybrid bowl shows a high OH intensity localized toward the piston center and above the step near the radial bumps (as in Figure 15 – a) caused by to the flame-to-flame interaction. Moreover, the OH tracing predicts the experimental luminosity signal for the re-entrant bowl within the bowl, that is again visible due to reduced soot content [36], confirming the soot impact on the OH* chemiluminescence acquisition.

At $\theta_4 = +31$ CAD aEOI of main event

Moving ahead in the combustion process, late in the cycle, the re-entrant bowl shows a more intense oxidation rate of the residual fuel (see Figure 9) and consequently the total OH mass rises over than the hybrid bowl, as outlined in Figure 14. In Figure 15 – a, the re-entrant bowl highlights the highest OH content which is mainly placed in the bowl center, where the swirl flow affects the oxidation process of the late stage (see Figure 12). On the contrary, for the hybrid bowl a significant OH reduction can be detected near the bowl center. Comparing these results with the experimental acquisitions of Figure 15 – b, a qualitative agreement can be highlighted. For the re-entrant design the higher OH concentration is within the bowl as for the CFD results. Instead, for the hybrid design the reduction of OH content respect to the re-entrant bowl is particularly evident. Some OH regions are still present near the cylinder periphery and this may be related to a faster oxidation rate for the hybrid bowl in the experimental tests, as it can be noted comparing the numerical (Figure 9) and the experimental (Figure 10) HRR during the late phase of the combustion process.
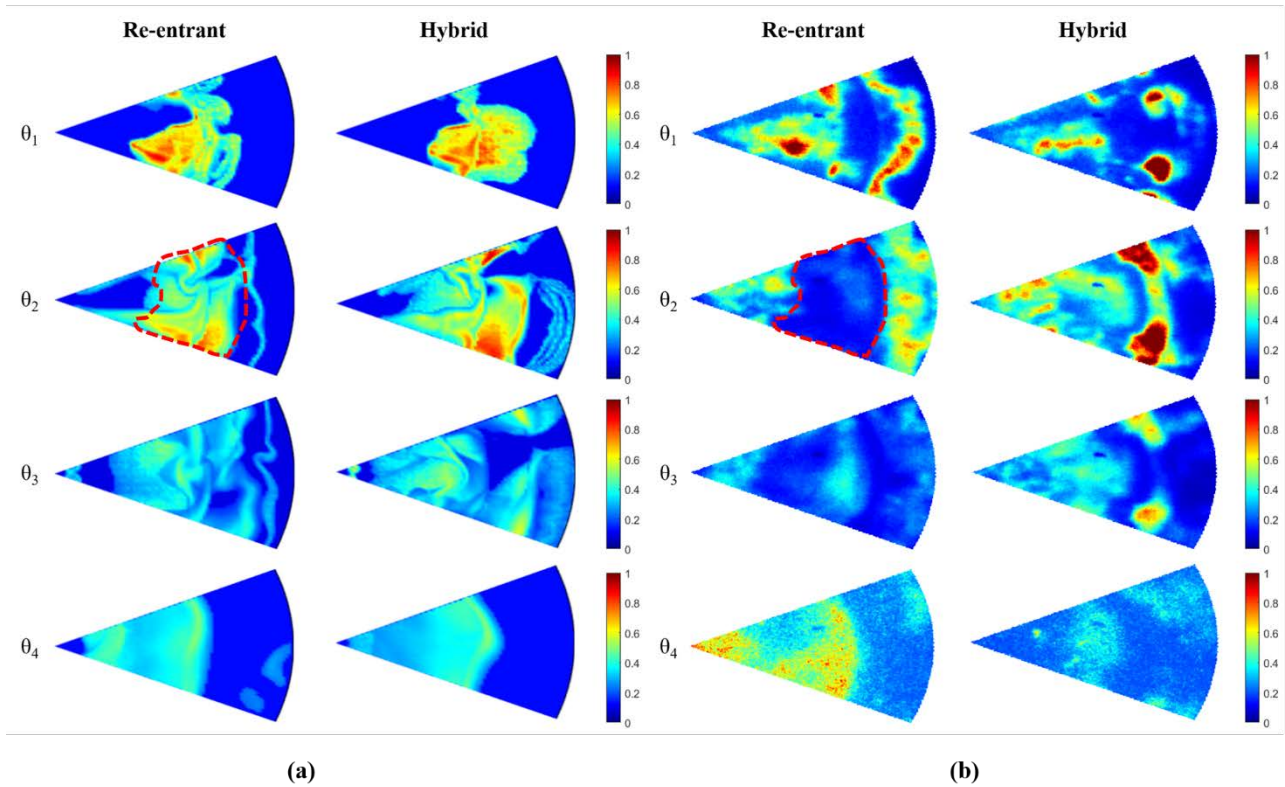
Figure 15. (a) 3D-CFD OH mass fraction averaged along the cylinder axis. Engine operating condition: 1500 RPM x 4.6 bar IMEP; (b) Experimental OH* chemiluminescence images. Engine operating condition: 1250 RPM x 4.5 bar IMEP

5. Conclusions

This work aims to analyse through numerical simulations and experimental data from optical engine, an innovative hybrid piston bowl, featuring both a highly-reentrant sharp-stepped bowl and a number of radial bumps in the inner bowl rim equal to the injector nozzle holes. This hybrid bowl was designed for a swirl-supported light-duty diesel engine and was compared with a conventional re-entrant bowl under partial load engine operating point. Firstly, a 3D-CFD investigation under non-reacting condition was carried out to understand the piston bowl effects on the air/fuel mixing process and on the main turbulent structures. Then, the numerical combustion outcomes were validated against the data coming from the optical access engine. For the scope, combustion image velocimetry (CIV) and the OH* chemiluminescence techniques were performed to evaluate, respectively, the kinematic analysis of the flame and the oxidation process in the near-stoichiometric region of the flame. The main outcomes of the research activity can be summarized as follow:

- Under non-reacting condition, the hybrid bowl showed a remarkable improvement of the air/fuel mixing process after the EOI of main injection. The strong interaction between the swirling flow and the radial bumps enabled different turbulent structures with respect to the re-entrant bowl. Firstly, the jet-to-jet interaction was highly

reduced, limiting the formation of fuel-rich zones and increasing the air entrainment onto the jet front. Moreover, the radial bumps coupled with lower swirl ratio leaded to better jet momentum redistribution on to the bowl surface. This resulted in higher jet recirculation toward the bowl center (reverse flow) where the available oxygen can effectively improve the air/fuel mixing on the leading edge of the jet.

- The combustion simulations have confirmed the mixing improvement for the hybrid bowl. Indeed, this latter design showed a more intense heat release rate (HRR) than for the re-entrant bowl after the EOI of main injection. While, in the late cycle, the higher residual fuel for the re-entrant bowl and the higher swirl ratio resulted in faster energy release. The numerical HRR showed a fairly good agreement with respect to the experimental HRR obtained for a similar engine operating condition.

- The average CFD velocity flow field well matched with the experimental CIV-resolved flow for both the piston bowls investigated. During the injection event, the hybrid bowl led to higher flame velocity close to the radial bumps region due to the faster flame propagation toward the cylinder center. Contrarily, in the conventional re-entrant bowl, the swirling flow represented the main flow structure, especially in the late cycle.

- The numerical OH distribution showed high predictivity in reproducing the OH* chemiluminescence images from the optical engines, except for some discrepancies due to the soot blackening, that has not be considered in the numerical OH computation. The hybrid bowl highlighted two high OH magnitude regions: one was placed in the squish region, the other was localized in the radial bumps zone and advanced toward the bowl center suggesting a better oxidation process in the near-stoichiometric region of the flame and thus faster combustion rate than with the re-entrant bowl.

Several outcomes of the presented study have highlighted the air/fuel mixing improvements for the proposed hybrid bowl, thus paving the way for a potential soot reduction without any detrimental effect on engine efficiency. Therefore, further analysis will be carried out on soot distribution, by the synergetic application of 3D-CFD and optical access engine experimental campaign. The 2-color pyrometry technique will be used to deeper understand the soot formation/oxidation mechanisms aiming to further optimization of the piston bowl design.

Abbreviations

AMR	Adaptive Mesh Refinement
CAD aEOI main	Crank Angle Degrees after End of Injection of Main Event
CAD aTDC	Crank Angle Degrees after Top Dead Center
CFD	Computational Fluid Dynamics
CI	Compression Ignition
CIV	Combustion Image Velocimetry
EGR	Exhaust Gas Recirculation
EOI	End of Injection
HRR	Heat Release Rate

ICE	Internal Combustion Engine
IMEP	Indicated Mean Effective Pressure
KH-RT	Kelvin Helmholtz and Rayleigh Taylor
NTC	No Time Counter
PAH	Poly-cyclic Aromatic Hydrocarbons
PIV	Particle Image Velocimetry
PM	Particulate Mimic
RANS	Reynolds-averaged Navier-Stokes
RNG	Re-Normalization Group
SOI	Start of Injection
SR	Swirl Ratio
TDC	Top Dead Center
VGT	Variable Geometry Turbine
yOH	OH mass fraction

References

1. Ritchie H. Sector by sector: where do global greenhouse gas emissions come from? Our World Data 2020. https://ourworldindata.org/ghg-emissions-by-sector (accessed September 23, 2020).

2. Kalghatgi, G., "Is it really the end of internal combustion engines and petroleum in transport?," Applied Energy 225:965-974, 2018, https://doi.org/10.1016/j.apenergy.2018.05.076.

3. Benajes, J., García, A., Monsalve-Serrano, J., and Lago Sari, R., "Fuel consumption and engine-out emissions estimations of a light-duty engine running in dual-mode RCCI/CDC with different fuels and driving cycles," Energy 157:19–30, 2018, https://doi.org/10.1016/j.energy.2018.05.144.

4. Boccardo, G., Millo, F., Piano, A., Arnone, L., Manelli, S., Fagg, S., Gatti, P., Herrmann, O.E., Queck, D., and Weber, J., "Experimental investigation on a 3000 bar fuel injection system for a SCR-free non-road diesel engine," Fuel 243:342–351, 2019, https://doi.org/10.1016/j.fuel.2019.01.122.

5. Benajes, J., Pastor, J. V., García, A., and Monsalve-Serrano, J., "An experimental investigation on the influence of piston bowl geometry on RCCI performance and emissions in a heavy-duty engine," Energy Convers. Manag. 103:1019–1030, 2015, https://doi.org/10.1016/j.enconman.2015.07.047.

6. Leach, F., Ismail, R., Davy, M., Weall, A., and Cooper, B., "The effect of a stepped lip piston design on performance and emissions from a high-speed diesel engine," Applied Energy 215:679–689, 2018, https://doi.org/10.1016/j.apenergy.2018.02.076.

7. Li, J., Yang, W.M., An, H., Maghbouli, A., and Chou, S.K., "Effects of piston bowl geometry on combustion and emission characteristics of biodiesel fueled diesel engines," Fuel 120:66–73, 2014, https://doi.org/10.1016/j.fuel.2013.12.005.

8.   Zha, K., Busch, S., Warey, A., Peterson, R. et al., "A Study of Piston Geometry Effects on Late-Stage Combustion in a Light-Duty Optical Diesel Engine Using Combustion Image Velocimetry," SAE Int. J. Engines 11(6):783-804, 2018, https://doi.org/10.4271/2018-01-0230.

9.   Zhang, T., Eismark, J., Munch, K., and Denbratt, I., "Effects of a wave-shaped piston bowl geometry on the performance of heavy duty Diesel engines fueled with alcohols and biodiesel blends," Renewable Energy 148:512–522, 2020, https://doi.org/10.1016/j.renene.2019.10.057.

10.   Eismark, J., Christensen, M., Andersson, M., Karlsson, A., and Denbratt, I., "Role of fuel properties and piston shape in influencing soot oxidation in heavy-duty low swirl diesel engine combustion," Fuel 254:115568, 2019, https://doi.org/10.1016/j.fuel.2019.05.151.

11.   Busch, S., Zha, K., Perini, F., Reitz, R. et al., "Bowl Geometry Effects on Turbulent Flow Structure in a Direct Injection Diesel Engine," SAE Technical Paper 2018-01-1794, 2018, https://doi.org/10.4271/2018-01-1794.

12.   Yoo, D., Kim, D., Jung, W., Kim, N. et al., "Optimization of Diesel Combustion System for Reducing PM to Meet Tier4-Final Emission Regulation without Diesel Particulate Filter," SAE Technical Paper 2013-01-2538, 2013, https://doi.org/10.4271/2013-01-2538.

13.   Smith, A., "Ricardo low emissions combustion technology helps JCB create the off-highway industry's cleanest engine," Ricardo Press Release (222915):4–6, 2010.

14.   Eder, T., Kemmner, M., Lückert, P., and Sass, H., "OM 654 – Launch of a New Engine Family by Mercedes-Benz," 18–25, 2016.

15.   Kurtz, E. and Styron, J., "An Assessment of Two Piston Bowl Concepts in a Medium-Duty Diesel Engine," SAE Int. J. Engines 5(2):344-352, 2012, https://doi.org/10.4271/2012-01-0423.

16.   Eismark, J., Andersson, M., Christensen, M., Karlsson, A. et al., "Role of Piston Bowl Shape to Enhance Late-Cycle Soot Oxidation in Low-Swirl Diesel Combustion," SAE Int. J. Engines 12(3):233-249, 2019, https://doi.org/10.4271/03-12-03-0017.

17.   Millo, F., Piano, A., Roggio, S., Bianco, A. et al., "Numerical Investigation on Mixture Formation and Combustion Process of Innovative Piston Bowl Geometries in a Swirl-Supported Light-Duty Diesel Engine," SAE Int. J. Engines 14(2):247-262, 2021, https://doi.org/10.4271/03-14-02-0015.

18.   Belgiorno, G., Boscolo, A., Dileo, G., Numidi, F. et al., "Experimental Study of Additive-Manufacturing-Enabled Innovative Diesel Combustion Bowl Features for Achieving Ultra-Low Emissions and High

Efficiency," SAE Int. J. Adv. & Curr. Prac. in Mobility 3(1):672-684, 2021, https://doi.org/10.4271/2020-37-0003.

19. Millo, F., Piano, A., Peiretti Paradisi, B., Marzano, M.R. et al., "Development and Assessment of an Integrated 1D-3D CFD Codes Coupling Methodology for Diesel Engine Combustion Simulation and Optimization," Energies 13:1612, 2020, https://doi.org/10.3390/en13071612.

20. Piano, A., Millo, F., Boccardo, G., Rafigh, M. et al., "Assessment of the Predictive Capabilities of a Combustion Model for a Modern Common Rail Automotive Diesel Engine," SAE Technical Paper 2016-01-0547, 2016, https://doi.org/10.4271/2016-01-0547.

21. Piano, A., Millo, F., Postrioti, L., Biscontini, G. et al., "Numerical and Experimental Assessment of a Solenoid Common-Rail Injector Operation with Advanced Injection Strategies," SAE Int. J. Engines 9(1):565-575, 2016, https://doi.org/10.4271/2016-01-0563.

22. Piano, A., Boccardo, G., Millo, F., Cavicchi, A. et al., "Experimental and Numerical Assessment of Multi-Event Injection Strategies in a Solenoid Common-Rail Injector," SAE Int. J. Engines 10(4):2129-2140, 2017, https://doi.org/10.4271/2017-24-0012.

23. Pastor, J.V., Olmeda, P., Martín, J., and Lewiski, F., "Methodology for Optical Engine Characterization by Means of the Combination of Experimental and Modeling Techniques," Applied Sciences. 2018; 8(12):2571. https://doi.org/10.3390/app8122571.

24. Orszag, S. A., Yakhot, V., Flannery, W. S., Boysan, F. et al., "Renormalization Group Modeling and Turbulence Simulations," Near-Wall Turbulent Flows 1993, 13, 1031–1046.

25. Richards, K. J., Senecal, P.K. and Pomraning, E., "Converge 2.3 Manual," Convergent Science Inc.: Madison, WI, USA, 2016.

26. Amsden, A.A., "KIVA-3V: A Block Structured KIVA Program for Engines with Vertical or Canted Valves," Los Alamos National Laboratory Technical Report LA-13313-MS, 1997.

27. Reitz, R.D. and Bracco, F.V., "Mechanisms of Breakup of Round Liquid Jets," Encyclopedia of Fluid Mechanism, 1986, 3, 233–249.

28. Amsden, A.A., O'Rourke, P.J., and Butler, T.D., "KIVA-II: A Computer Program for Chemically Reactive Flows with Sprays," Los Alamos National Laboratory Technical Report LA-11560-MS, 1989.

29. Schmidt, D.P. and Rutland, C.J., "A New Droplet Collision Algorithm," Journal of Computational Physics, Volume 164, Issue 1, 2000, Pages 62-80, ISSN 0021-9991, https://doi.org/10.1006/jcph.2000.6568.

30. O'Rourke, P. and Amsden, A., "The Tab Method for Numerical Calculation of Spray Droplet Breakup," SAE Technical Paper 872089, 1987, https://doi.org/10.4271/872089.

31. O'Rourke, P. and Amsden, A., "A Spray/Wall Interaction Submodel for the KIVA-3 Wall Film Model," SAE Technical Paper 2000-01-0271, 2000, https://doi.org/10.4271/2000-01-0271.

32. Frenklach, M. and Wang, H., "Detailed Modeling of Soot Particle Nucleation and Growth," Symposium (International) on Combustion, Volume 23, Issue 1, 1991, Pages 1559-1566, ISSN 0082-0784, https://doi.org/10.1016/S0082-0784(06)80426-1.

33. Kazakov, A., Wang, H., and Frenklach, M., "Detailed modeling of soot formation in laminar premixed ethylene flames at a pressure of 10 bar," Combustion and Flame, Volume 100, Issues 1–2, 1995, Pages 111-120, ISSN 0010-2180, https://doi.org/10.1016/0010-2180(94)00086-8.

34. Kazakov, A. and Frenklach, M., "Dynamic Modeling of Soot Particle Coagulation and Aggregation: Implementation With the Method of Moments and Application to High-Pressure Laminar Premixed Flames," Combustion and Flame, Volume 114, Issues 3–4, 1998, Pages 484-501, ISSN 0010-2180, https://doi.org/10.1016/S0010-2180(97)00322-2.

35. Zeuch, T., Moréac, G., Ahmed, S.S. and Mauss, F., "A comprehensive skeletal mechanism for the oxidation of n-heptane generated by chemistry-guided reduction," Combustion and Flame, Volume 155, Issue 4, 2008, Pages 651-674, ISSN 0010-2180, https://doi.org/10.1016/j.combustflame.2008.05.007.

36. Pastor, J. V., García, A., Micó, C., and Lewiski, F., "Soot reduction for cleaner Compression Ignition Engines through innovative bowl templates," International Journal of Engine Research 1–15, 2020, https://doi.org/10.1177/1468087420951324.

37. Payri, F., Olmeda, P., Martín, J., and García, A., "A complete 0D thermodynamic predictive model for direct injection diesel engines," Applied Energy 88(12):4632–4641, 2011, https://doi.org/10.1016/j.apenergy.2011.06.005.

38. Thielicke, W. and Stamhuis, E.J., "PIVlab – Towards User-friendly, Affordable and Accurate Digital Particle Image Velocimetry in MATLAB," J. Open Res. Softw. 2, 2014, http://doi.org/10.5334/jors.bl.

39.   Perini, F., Zha, K., Busch, S., Kurtz, E. et al., "Piston geometry effects in a light-duty, swirl-supported diesel engine: Flow structure characterization," International Journal of Engine Research, 19(10):1079–1098, 2018, https://doi.org/10.1177/1468087417742572.

40.   Dembinski, H., Angstrom, H., and Razzaq, H., "In-Cylinder Flow Pattern Evaluated with Combustion Image Velocimetry, CIV, and CFD Calculations during Combustion and Post-Oxidation in a HD Diesel Engine," SAE Technical Paper 2013-24-0064, 2013, https://doi.org/10.4271/2013-24-0064.